Laser & Photonics Reviews

LASER & PHOTONICS REVIEWS

www.lpr-journal.org

RESEARCH ARTICLE

Colloidal Quantum Wells Enable Phototransistors with Enhanced Visible Light Detection

Ziqing Liu[1,2] | Emek Goksu Durmusoglu[3] | Yunfei Ren[4] | Peng Xiao[1] | Wenhui Fang[4] | Haixing Tan[1] | Haojun Zhang[1] | Xiaoguang Lin[1] | Yi Dai[5] | Sui-Dong Wang[6,7] | Chuan Liu[4] | Pedro Ludwig Hernandez-Martinez[3] | Corentin Dabard[3] | Dongxu Zhao[1] | Hilmi Volkan Demir[3,8] | Baiquan Liu[4]

[1]School of Physics and Optoelectronic Engineering, Guangdong-Hong Kong-Macao Joint Laboratory of Intelligent Micro-Nano Optoelectronic Technology, Foshan University, Foshan, Guangdong, China | [2]School of Electronic Information Engineering, Foshan University, Foshan, Guangdong, China | [3]Luminous! Center of Excellence for Semiconductor Lighting and Displays, School of Electrical and Electronic Engineering, School of Physical and Mathematical Sciences, School of Materials Science and Engineering, Nanyang Technological University, Singapore, Singapore | [4]Guangdong Provincial Key Laboratory of Display Materials and Technologies, State Key Laboratory of Optoelectronic Materials and Technologies, School of Electronics and Information Technology, Sun Yat-sen University, Guangzhou, China | [5]School of Education, City University of Macau, Macau, China | [6]Institute of Functional Nano and Soft Materials (FUNSOM), Jiangsu Key Laboratory for Carbon-Based Functional Materials and Devices, Soochow University, Suzhou, Jiangsu, China | [7]Macao Institute of Materials Science and Engineering (MIMSE), Macau University of Science and Technology, Taipa, Macao, China | [8]Department of Electrical and Electronics Engineering and Department of Physics, UNAM-Institute of Materials Science and Nanotechnology and the National Nanotechnology Research Center, Bilkent University, Bilkent, Ankara, Turkey

Correspondence: Peng Xiao (xiaopeng@fosu.edu.cn) | Dongxu Zhao (zhaodx@fosu.edu.cn) | Hilmi Volkan Demir (hvdemir@ntu.edu.sg) | Baiquan Liu (liubq33@mail.sysu.edu.cn)

Received: 11 July 2025 | **Revised:** 26 September 2025 | **Accepted:** 13 October 2025

Keywords: colloidal quantum wells | energy-band engineering | InGaZnO | phototransistors | visible light detection

ABSTRACT

InGaZnO (IGZO) phototransistors have largely attracted research attention due to their excellent electrical properties. However, the wide bandgap (>3.0 eV) of IGZO phototransistors intrinsically limits their spectral response to UV wavelengths, hindering their applicability in visible-light optoelectronics. We report integrating colloidal quantum wells (CQWs, spin-coated at room temperature in ambient air) to extend the spectral sensitivity of IGZO phototransistors into the visible range. The resulting CQW/IGZO heterojunction phototransistor exhibits a six-order-of-magnitude enhancement in specific detectivity ($D^* = 1 \times 10^{11}$ Jones at 660 nm) across the visible spectrum (405–660 nm), while retaining excellent electrical performance, including a maximum mobility of 13.38 $cm^2\ V^{-1}\ s^{-1}$ and an on/off current ratio of 1.53×10^9. Energy-band engineering at the CQW/IGZO interface, with a conduction band offset ($\Delta E_c = 0.15$ eV), facilitates efficient charge separation and promotes electron injection into the IGZO channel. Gate-modulation further enables the device to drive quantum-dot light-emitting diodes, underscoring its potential in adaptive sensing and integrated optoelectronics. This work demonstrates the integration of CQWs in thin-film transistors as a scalable and cost-effective strategy to broaden the optoelectronic functionality of wide-bandgap semiconductors.

1 | Introduction

The rapid advancement of technologies such as electronic communication, the Internet of Things (IoT), and intelligent driving systems has spawned a surge in demand for photodetectors in a wide range of interactive applications [1]. In particular, photodetectors have a unique mechanism for converting optical signals into electrical signals and are therefore widely used in

Ziqing Liu, Emek Goksu Durmusoglu, and Yunfei Ren contributed equally to this work.

mobile wearables, self-driving cars, medical imaging, and optical sensing. Among available technologies, phototransistors offer distinct advantages over traditional photoresistors and photodiodes by enabling signal amplification through gate modulation, making them promising candidates for high-performance optical sensing applications [2–6].

While organic phototransistors (OPTs) offer flexibility and lightweight, they suffer from instability, slow response, and large-area fabrication challenges [7]. In contrast, InGaZnO (IGZO) phototransistors have attracted the attention of researchers due to their electrical properties of high mobility, low off-state current (I_{off}) combined with good uniformity and large area integration [8–12]. However, the wide bandgap of IGZO (>3.0 eV) limits its spectral response to the UV range [13, 14], thereby constraining its applications in visible-light optoelectronics.

To address this spectral limitation, various light-absorbing materials have been integrated into IGZO-based heterojunction phototransistors, including chalcogenides [15], perovskites [16, 17], organics [18], and quantum dots (QDs) [19, 20]. Despite improving visible-light sensitivity, QDs and perovskites often suffer from issues including environmental instability and degradation under prolonged illumination [21]. In contrast, 2D colloidal quantum wells (CQWs) have emerged as compelling alternatives due to their ultranarrow photoluminescence (PL) emission [22], high absorption cross-sections [23], and very high exciton binding energies [24], arising from their anisotropic shapes and 1D quantum confinement in the thickness direction. These features make CQWs attractive candidates for optoelectronic devices, yet their integration with phototransistors remains unexplored [25].

Among various CQWs heterostructures, type-II CdSe/CdTe/CdSe multicrown CQWs are especially suited for photodetection due to their staggered band alignment, which spatially separates photoexcited electrons (in the CdSe layers) and holes (in the CdTe layer) [26–28]. This spatial separation significantly extends carrier lifetimes, which is highly desirable for phototransistor operation. The resulting prolonged carrier dynamics enhances charge extraction efficiency and photocurrent generation, while the internal electric field promotes efficient exciton dissociation and electron injection into the IGZO channel, even under low gate bias. These characteristics make type-II CQWs particularly well-suited as visible-light sensitizers in wide-bandgap oxide phototransistors, where both high detectivity and strong photoresponse are critical.

In this study, we facilitate efficient charge separation through energy-band engineering at the CQWs/IGZO interface. We fabricate a heterojunction phototransistor by spin-coating CdSe/CdTe/CdSe CQWs onto IGZO films under ambient conditions. The resulting device exhibits remarkable electrical performance, including a maximum mobility (μ_{max}) of 13.38 $cm^2V^{-1}s^{-1}$, a subthreshold swing (SS) of 0.12 V/decade, and an on/off current ratio (I_{on}/I_{off}) of 1.53×10^9. The phototransistor-driven quantum-dot light-emitting diodes (QLED) integration demonstrates its excellent electrical performance through gate-modulated electroluminescence. In addition, compared to single-layer IGZO phototransistors, the spectra of the heterojunction phototransistor were broadened to red light (660 nm) with a specific detectivity of 1×10^{11} Jones. Subsequently, the effects of different gate pressures on the pulsed photoresponse were explored. This work provides a promising pathway for enhancing the visible-light sensitivity of wide-bandgap metal-oxide phototransistors using CQW-based heterojunction design.

2 | Results

2.1 | Device Design and Morphology

Figure 1A presents the fabrication process of the CQWs/IGZO heterojunction phototransistor. The key steps involve: (i) optimizing stable IGZO thin-film phototransistors via magnetron-sputtering, and (ii) subsequently, ambient spin-coating of the CQW layer to form the heterojunction. Figure 1B presents a top-view scanning electron microscopy (SEM) image of the IGZO thin-film active layer, revealing a compact and uniform morphology, free from pinholes and protrusions. This homogeneous microstructure (Figure S1A) is crucial for ensuring electrical stability, a prerequisite for high-performance device operation. Figure S1B displays a cross-sectional SEM image of the CQWs/IGZO heterojunction, clearly showing the bilayer structure: the IGZO layer is approximately 40 nm, and the spin-coated CQWs layer is ~15 nm.

Figure 1C presents the surface morphology of the CQWs/IGZO heterojunction, revealing uniform CQWs coverage across the IGZO surface, indicating the excellent compatibility between materials and the homogeneity achieved during the spin-coating process. The structural characteristics of the CdSe/CdTe/CdSe CQWs were further characterized via high-angle annular dark-field scanning transmission electron microscopy (HAADF-STEM), as shown in Figure 1F and Figure S2A,B. The CdSe/CdTe/CdSe CQWs exhibit average lateral dimensions of 16.8 ± 0.4 nm in width and 14.8 ± 0.3 nm in length. The CQWs were intentionally engineered to be smaller and squarish shape to achieve higher packing density, smoother, and pinhole-free film [22]. Figure S2C,D shows the calculated electron and hole wavefunctions of the CdSe/CdTe/CdSe CQWs. As seen, electrons localize in the CdSe core and CdSe outer crown, while holes are confined to the CdTe crown, confirming a type-II band alignment that drives exciton dissociation, prolongs carrier lifetimes, and facilitates efficient charge extraction in the IGZO/CQW device [26–28].

Figure 1D illustrates the 3D schematic diagram of the CQWs/IGZO heterojunction phototransistor, designed with a bottom-gate-top-contact architecture. The device incorporates 200 nm indium tin oxide (ITO) as the source-drain electrode, offering excellent electrical conductivity, optical transparency, and outstanding chemical stability [29]. A 200 nm Al_2O_3 ensures the low off-state current characteristics, while a 300 nm Al electrode provides reliable contact with the dielectric interface (see the Experimental Section for full fabrication details). Device operation involves applying a source-drain voltage (V_{DS}) and a gate voltage (V_{GS}) in combination with a pulse-controlled laser source. Figure 1E illustrates the integration of the phototransistor with a QLED, where the source is connected to the QLED anode and the cathode grounded. Gate and source biases (0–20 V) are independently controlled to modulate device behavior. Figure S3 presents the optical microscope image of the fabricated

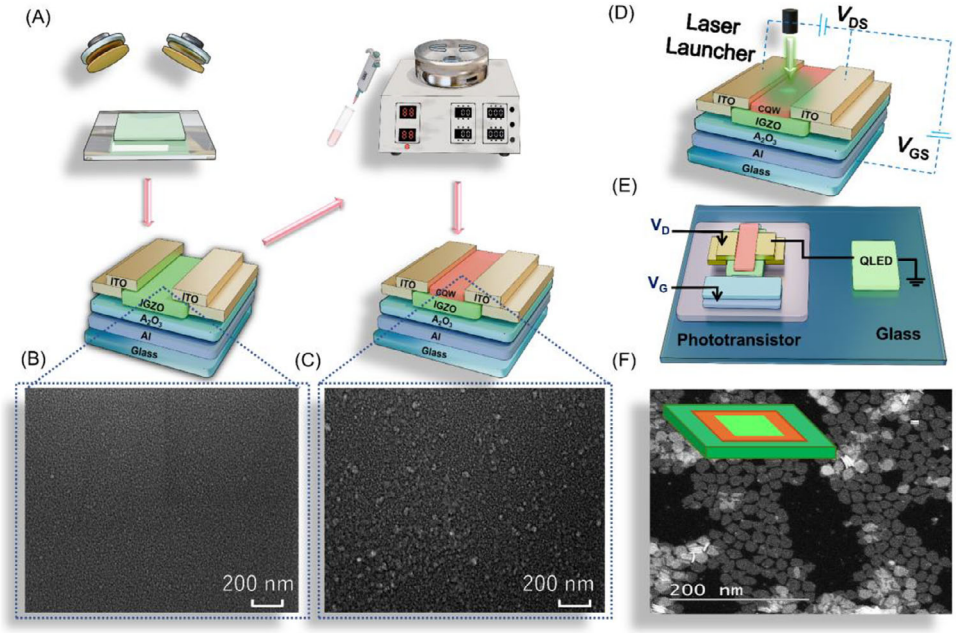

FIGURE 1 | (A) Schematic illustration of the fabrication process for the CQWs/IGZO heterojunction phototransistor; (B) Top-view SEM image of IGZO; (C) Top-view SEM image of CQWs/IGZO heterojunction; (D) The 3D schematic diagram of the CQWs/IGZO heterojunction phototransistor; (E) Circuit diagram showing the phototransistor integrated with a QLED for gate-controlled emission. (F) HAADF-TEM image of CdSe/CdTe/CdSe CQWs with an Inset schematic illustrating inner CdSe (bright green), CdTe layer (orange), and outer CdSe (dark green) layers. The stripe drawing illustrates the lateral cross-section of CQWs, which is shown with a dotted area in the schematic.

phototransistor, which has a channel length and width of 300 μm each.

2.2 | Electrical Performance and Photoresponse Characterization of Designed Phototransistors

In order to investigate the effect of device architecture on the performance of CQWs/IGZO heterojunction phototransistors, three device configurations were designed, as shown in Figure 2A–C. Device 1 (Figure 2A) serves as a control and consists of a standard IGZO thin-film transistor (IGZO-TFT) without any CQW layer. Device 2 (Figure 2B) incorporates a CQW layer spin-coated on top of the IGZO active layer, which was deposited via magnetron sputtering and annealed at 300 °C in ambient atmosphere for 30 min prior to CQW deposition. Device 3 (Figure 2C) shares the same process steps as Device 2, the sequence of CQW deposition and ITO electrode formation is reversed. ITO is deposited first, followed by spin-coating of the CQWs. The 300°C annealing process is considered essential for IGZO (In-Ga-Zn-O) thin films, as it effectively reduces the oxygen vacancy concentration within the semiconductor material through thermal-induced structural reorganization, which is verified through X-ray photoelectron spectroscopy (XPS) characterization (Figure S4).

Figure 2D shows the transfer characteristic curves of all three devices measured at a fixed V_{DS}. The current of the phototransistor is controlled by V_{GS} and V_{DS} together during the operation, and the magnitude of the current I_{DS} in the active layer varies with the change of V_{GS} under the same V_{DS}. As shown in Figure 2D, the transfer characteristics of Device 3 closely resemble those of Device 1, indicating minimal gate leakage and a well-defined turn-on voltage. In contrast, Device 2 exhibits a significantly larger gate leakage current and a positively shifted turn-on voltage, suggesting disrupted charge transport at the electrode-semiconductor interface. The current on/off ratio (I_{on}/I_{off}) is a key figure of merit for evaluating a device's switching capability. For flat panel displays (FPDs) applications, I_{off} must be below 10^{-12} A, and I_{on}/I_{off} ratio should be at least 10^6 [30, 31].

Figure 2E shows the I_{on}/I_{off} ratio of the three devices in dot-line representations. Device 2 demonstrates notably inferior electrical performance with an I_{on}/I_{off} ratio of 6.6×10^6 (Table 1), which is significantly lower than those of Devices 1 and 3. The low value may originate from the unfavorable placement of the CQWs layer between ITO and IGZO, which disturbs the electrode-semiconductor contact and introduces additional interfacial traps. These traps increase the I_{off} and cause a positive shift in V_{on}, as summarized in Table 1. Consequently, the degraded switching capability and elevated I_{off} in Device 2 can be attributed to trap-assisted conduction at the CQWs/IGZO interface. To evaluate charge trapping-induced hysteresis, bidirectional transfer characteristics were measured. Devices 1 and 3 exhibit negligible hysteresis, with ΔV_{GS} of 0.023 and 0.098 V, respectively, at a drain current (I_{DS}) of 5×10^{-8} A. In contrast, Device 2 shows a substantially larger hysteresis window of 0.70 V. The minimal hysteresis observed in Device 3 is consistent with its superior I_{on}/I_{off} ratio and lower *SS*. Furthermore, the reliability of these findings is supported by the gate leakage current measurements of all three devices (Figure S5).

Figure 2F compares carrier mobilities. All devices exhibited excellent electrical performance, with a μ_{max} of ~ above 10 $cm^2V^{-1}s^{-1}$, as detailed in Table 1. To further demonstrate the

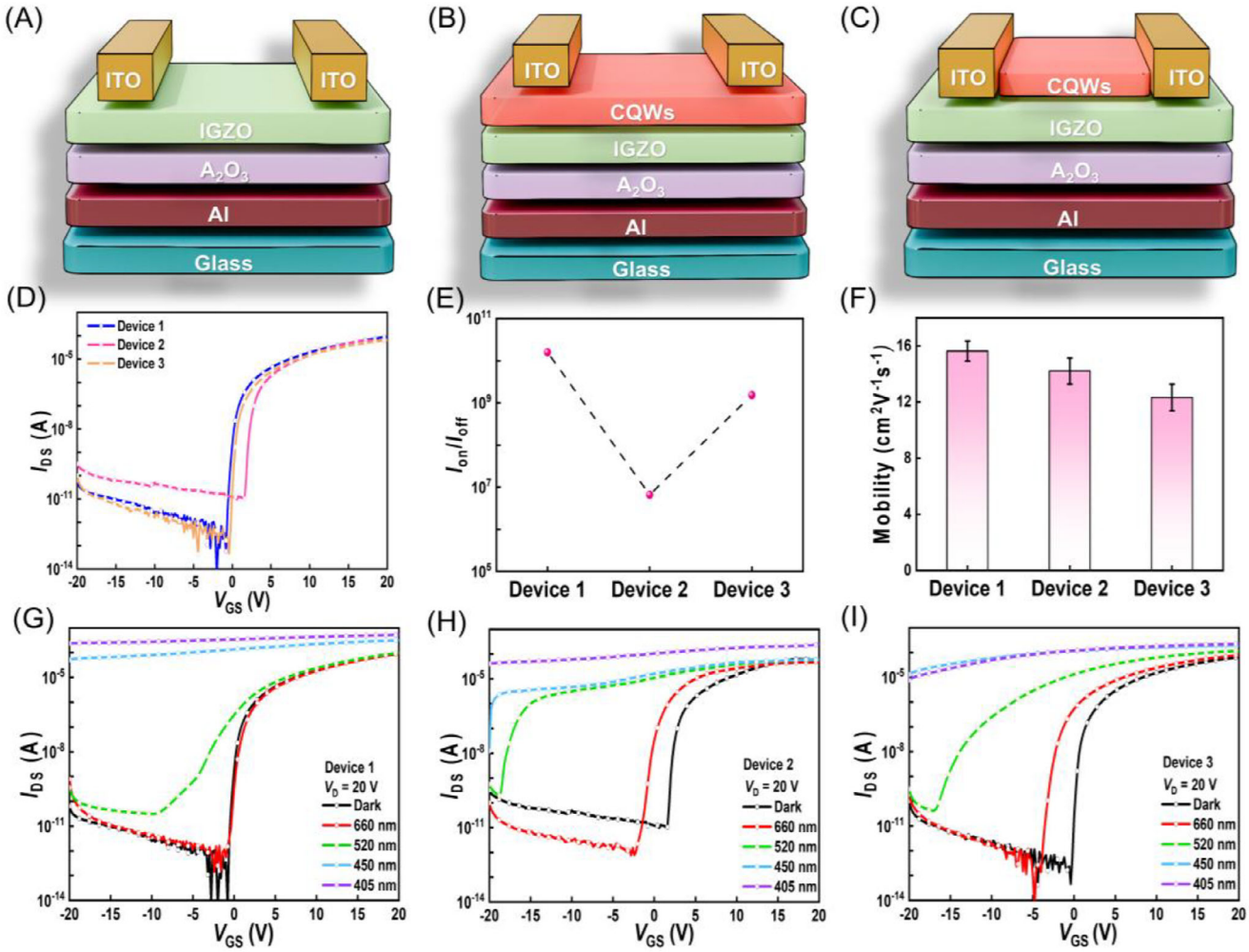

FIGURE 2 | (A–C) Schematic structure of three device configurations; (D) Transfer characteristic curves of three devices at fixed V_{DS}; (E) Comparison of I_{on}/I_{off} ratios; (F) Histogram of maximum mobility of three devices; (G–I) transfer curves under illumination of different wavelengths (V_{DS} = 20 V, λ = 660 m, 520 nm, 450 nm, 405 nm, P = 2 mW mm^{-2}) for three devices.

TABLE 1 | Electrical properties of the three phototransistor devices.

	μ_{max} (cm^{2}V^{-1}s^{-1})	I_{on}/I_{off}	SS (V•Decade^{-1})	V_{omn} (V)
Device 1	16.44	1.59×10^{10}	0.073	−0.85
Device 2	14.76	6.60×10^{6}	0.166	1.14
Device 3	13.38	1.53×10^{9}	0.126	−0.36

reliability and reproducibility of our IGZO phototransistor fabrication process, Figure S6 presents transfer curves and mobility histograms collected from multiple devices, showing an average mobility of 14.17 cm^{2}V^{-1}s^{-1}, highlighting the robustness of our IGZO phototransistors. Table 1 summarizes the key electrical properties of all three devices. Device 1, serving as the reference IGZO-TFT, delivers a high mobility and excellent I_{on}/I_{off} ratio. Interestingly, Device 2, despite its degraded switching behavior, exhibits the highest mobility of 14.76 cm^{2}V^{-1}s^{-1}, but with a significantly lower I_{on}/I_{off} ratio of 6.60 × 10^6. In contrast, Device 3 demonstrates a balanced performance with a mobility of 13.38 cm^{2}V^{-1}s^{-1}, and a superior I_{on}/I_{off} ratio of 1.53 × 10^9. These distinct electrical characteristics underscore the critical influence of fabrication sequence—particularly the positioning of the CQW layer relative to the ITO electrodes—on charge transport, contact resistance, and overall device performance. The results validate that appropriate structural design and material integration are key to optimizing heterojunction phototransistor performance.

Figure 2G–I shows the photoresponse characteristics of these three phototransistors (Device 1, Device 2, and Device 3), evaluated under laser irradiation at varying wavelengths (λ = 660, 520, 450, and 405 nm) with a fixed V_{DS} = 20 V and a constant light power density of 2 mW mm^{-2}. Transfer curves were recorded under each illumination condition to assess the spectral response.

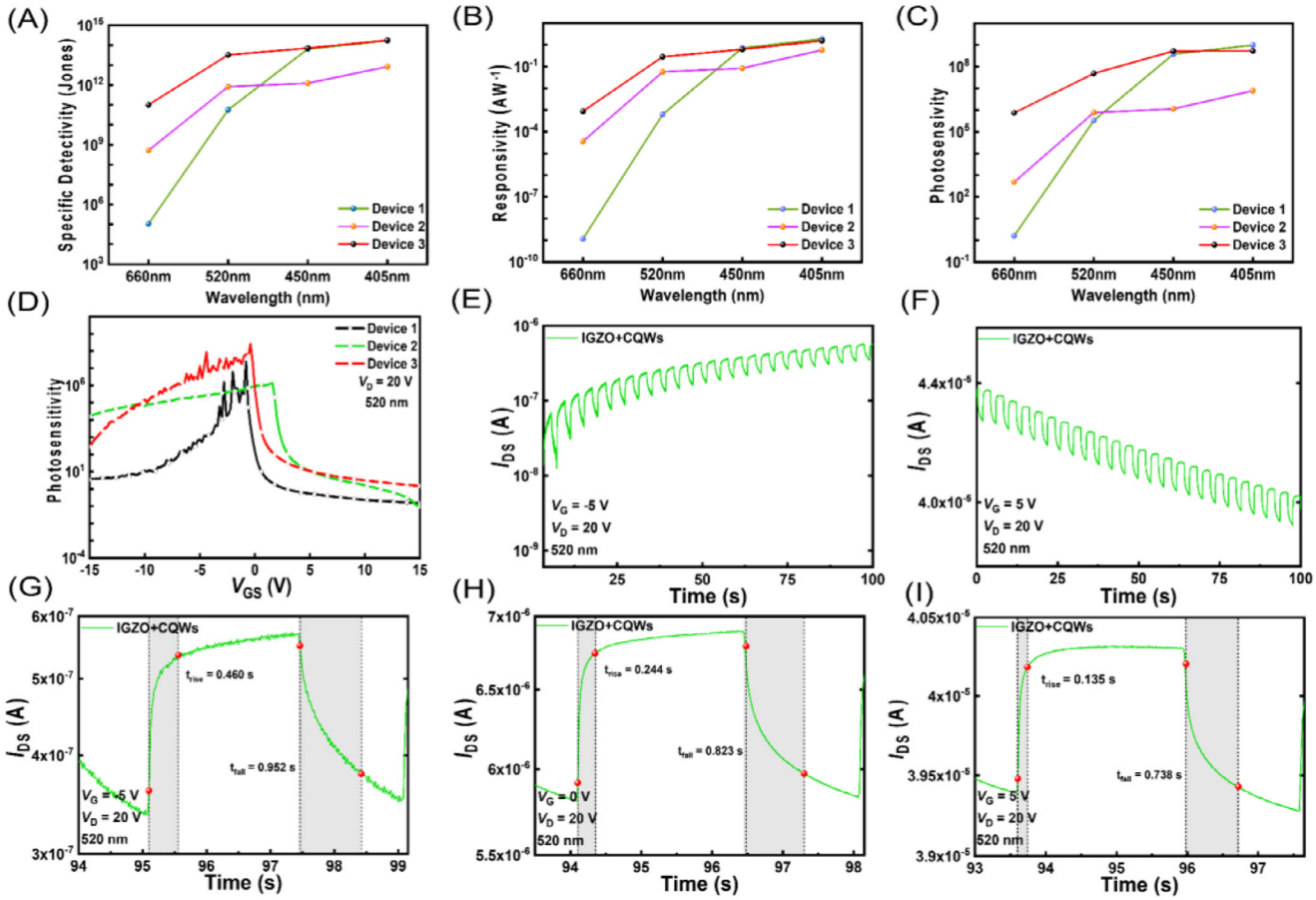

FIGURE 3 | (A–C) Wavelength-dependent specific detectivity (D^*), responsivity (R) and photosensitivity (PS) of the three devices; (D) PS trends of three devices under 520 nm illumination as a function of V_{GS}; (E,F) Long-term photoresponse of Device 3 under gate biases of −5 and 5 V, respectively (V_{DS} = 20 V, λ = 520 nm); (G–I) Rise/fall time of device 3 under gate bias from −5 to 5 V (V_{DS} = 20 V, λ = 520 nm).

As shown in Figure 2G, Device 1, the bare IGZO-TFT, exhibits a noticeable photocurrent under green light illumination (λ = 520 nm), yet remains insensitive to red light (λ = 660 nm). This limited spectral response is attributed sub-bandgap states induced by oxygen vacancies generated during the magnetron sputtering process. These defects may alter the photoresponse range of the IGZO phototransistor [32]. In contrast, Device 2 and Device 3, both incorporating CQWs as light-absorbing layer, exhibit a pronounced photoresponse even under red light illumination (λ = 660 nm), as shown in Figure 2H,I, respectively. The enhanced response is due to the efficient light absorption by the type-II CQWs and the effective charge transfer into the IGZO channel. Notably, the CQW layer was deposited under ambient air atmosphere rather than in an inert gas environment. This demonstrates the robustness of the CQW layer, highlighting a wide process window that is advantageous for scalable and cost-effective fabrication.

2.3 | Enhanced Visible-Light Photoresponse and Gate-Modulated Behavior

Figure 3A–C compares the responsivity (R), photosensitivity (PS), and specific detectivity (D^*) of three devices under constant illumination at various wavelengths (λ = 660, 520, 450, and 405 nm). Overall, Device 3 exhibits superior photoresponse performance, especially across the visible spectrum. Whereas Device 2 exhibited a notable enhancement in D^* over Device 1 in the longer wavelength range (520 nm and 660 nm), which can be ascribed to the effective light absorption provided by the CQW layer. While Device 3 outperforms both alternatives across most wavelengths, Device 1 retains relatively higher sensitivity at shorter wavelengths (405 and 450 nm).

The D^* of Device 3 reaches 1.01×10^{11} and 3.27×10^{13} Jones at 660 and 520 nm, respectively (Figure 3A), which is 6 and 3 orders of magnitude higher Device 1. In addition, Device 2 exhibits improved D^*, achieving increases 3 and 1 orders of magnitude at 660 and 520 nm, respectively, compared to Device 1.

As shown in Figure 3B,C, Device 2 significantly outperforms Device 1 in both R and PS across all four tested wavelengths. As shown in the supporting Table S1, the R of Device 2 is up to 4 orders of magnitude higher at 660 nm and 2 orders at 520 nm, compared to Device 1. A similar trend is observed in PS, highlighting the potential of CQWs to significantly enhance long-wavelength photoresponse in IGZO-based phototransistors. The R, PS, and D^* can be obtained by the formulas of

$$R = \frac{I_{photo} - I_{dark}}{P \times A} \quad (1)$$

$$PS = \frac{I_{photo} - I_{dark}}{I_{dark}} \quad (2)$$

$$D^* = \frac{R \cdot \sqrt{A}}{\sqrt{2qI_{dark}}} \quad (3)$$

where P is the incident light intensity, A is the effective area, q is the electronic charge, and I_{dark} is dark current [33, 34].

Figure 3D shows the PS trends of all three devices under green light illumination (λ = 520 nm) as a function of V_{GS} Device 3 consistently achieves the highest PS values, indicating excellent stability and enhanced photodetection rate under green light illumination. Notably, all devices reach their peak PS value just before the threshold turn-on voltage, likely due to a higher number of photoexcited charge carriers relative to bias-induced charge carriers in the turn-off state, where the V_{GS} is smaller than the turn-on voltage. On the other hand, when the device is in the turn-on state, the relative contribution of bias-induced charge carriers exceeds that of photoexcited charge carriers, resulting in a decrease in PS. Therefore, the contribution of photoexcited and bias-induced carriers to the channel current varies with V_{GS}, leading to different trends in PS.

Figure 3E,F presents the long-term photoresponse of the device under V_{GS} of −5 and +5 V, respectively. Under a constant negative V_{GS} the device exhibits a pronounced increase in photocurrent in response to light pulse stimulation. Specifically, when illuminated with 520 nm light pulses at a frequency of 0.25 Hz for 100 s, the photocurrent of the phototransistor rises from an initial value of 10^{-8} A to approximately 10^{-6} A. Conversely, under a constant positive V_{GS}, the photocurrent gradually decreases from 4.4×10^{-5} to 3.9×10^{-5} A in 100 s under the same illumination, indicating gate-controlled suppression of photogenerated carriers.

Figure 3G–I provides rise/fall times under pulsed illumination for bandwidth analysis. The rise and fall times, defined as the time to change from 10% to 90% and vice versa, were extracted from the photocurrent dynamics. With V_{GS} tuned from −5 to +5 V, the rise time shortens from 0.46 to 0.135 s, while the fall time decreases from 0.952 to 0.738 s. Correspondingly, the bandwidth is enhanced from 0.76 to 2.6 Hz (The bandwidth, estimated as $f_{3dB} = 0.35/t_{rise}$). These results indicate the device's potential for tunable, gated multimode operation, although the speed is still not fast enough.

To further quantify the trap density and energy distribution associated with carrier trapping in the persistent photoconductivity (PPC) effect, a bi-exponential fitting was performed on the decaying photocurrent in Figure 3G. According to Equation (4), a bi-exponential fitting of the photocurrent decay curve (Figure S7) was employed to quantitatively deconvolute the trap states. The fitting yielded two distinct time constants: τ_1 = 77.1 ms and τ_2 = 884 ms. The fast time constant (τ_1) is associated with the rapid release of carriers from shallow traps, while the slow time constant (τ_2) is a signature of carrier detention in deep traps, which governs the observed persistent photoconductivity. The considerable magnitude of the τ_2 component indicates a high density of such deep traps within the material. And the detailed parameters obtained from the bi-exponential fitting are listed in Table S4.

$$I_{(t)} = I_0 + A_1 e^{-\frac{t}{\tau_1}} + A_2 e^{-\frac{t}{\tau_2}} \quad (4)$$

These results indicate that the phototransistor's response is sensitive to the combined effects of V_{GS} and illumination. On the one hand, negative V_{GS} enhances the built-in electric field at the CQWs/IGZO heterojunction, promoting efficient separation of photogenerated carriers and amplifying the photocurrent. In contrast, the positive V_{GS} eliminates this effect by opposing the light-induced field, particularly under weak illumination conditions and high positive voltages [35]. Figure S8 shows the pulsed light response profile of CQWs/IGZO heterojunction phototransistors at all four tested wavelengths.

2.4 | Heterojunction Design and Charge Transfer Mechanism

Figure 4A shows the absorption spectra IGZO and CQWs, along with the PL profile of the CQWs. The distinct absorption peaks at 481 and 513 nm in the CQWs spectrum confirm strong quantum confinement effects inherent to their quasi-2D geometry. Notably, the CQW layer exhibits sharp and narrow PL features, as shown in Figure S9, which further supports their high exciton binding energy and suitability for optoelectronic applications. According to the Tauc plot analysis of absorption spectra (Figure S10), the optical bandgap (E_g) values were determined as 3.47 eV for IGZO and 2.39 eV for heavy hole transition (513 nm) for CQWs and 2.1 eV for type-II transition (590 nm), respectively.

Figure 4B illustrates the energy band alignment of the IGZO/CQWs heterojunction. Ultraviolet photoelectron spectroscopy (UPS) measurements were performed using a He I discharge lamp (with a photon energy of 21.22 eV) to extract both the secondary electron cutoff (SEC) and valence band maximum (VBM) spectra. As shown in Figure S11, the measured work function values of IGZO and CQWs are 4.75 and 4.60 eV, respectively (in Supporting Information). The valence band edge to Fermi level (E_v - E_f) positions were quantified as −2.63 eV (IGZO) and −1.00 eV (CQWs), respectively. By combining these values with the derived E_g values, the conduction band edge to Fermi level (E_c - E_f) are calculated as 0.84 eV for IGZO (E_g = 3.47 eV) and 1.1 eV for CQWs (E_g = 2.1 eV), respectively. This analysis reveals a conduction band offset ΔE_c = 0.41 eV and a valence band offset ΔE_v = 1.78 eV at the IGZO/CQWs interface, confirming favorable energy-level alignment for charge transport and phototransistor operation.

Figure 4C,D schematically depicts the charge transport mechanisms of the CQWs/IGZO phototransistor under different V_{GS} regimes. Without light excitation (dark), due to the low carrier concentrations, the CQW layer has a negligible influence on charge transfer, and the I_D arises primarily from the IGZO layer. Upon illumination, the CQW layer generates electron–hole pairs through photoexcitation. Owing to the built-in electric field and favorable energy-level alignment, photogenerated electrons at CQW layer are transferred to the IGZO layer while holes remain confined in the CQW layer due to the valence band offset. This

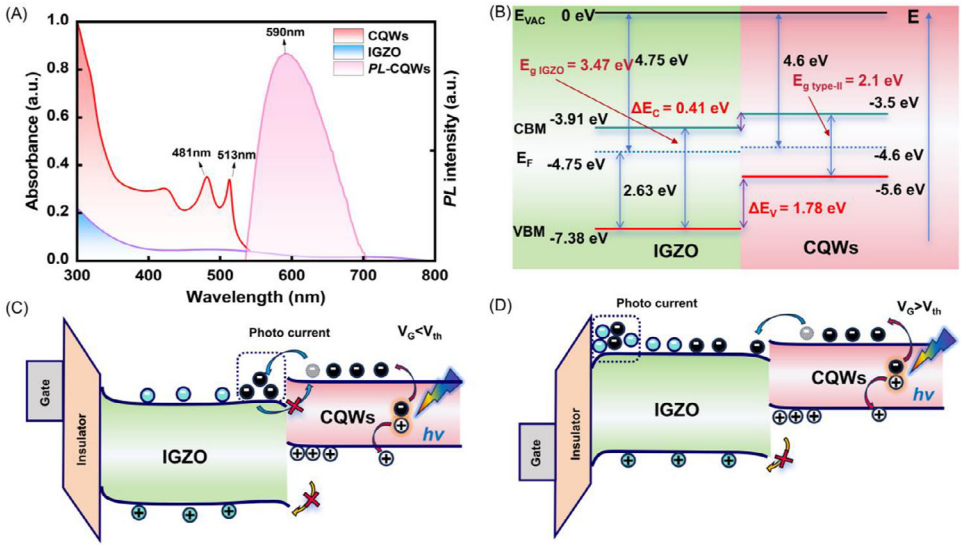

FIGURE 4 | (A) The absorption spectra of IGZO with CQWs, along with PL spectra of CQW; (B) The energy band diagrams of IGZO/CQWs heterojunction based on UPS and Tauc analysis; (C,D) Schematic of carrier transport photogeneration mechanisms for $V_{GS} < V_{th}$ and $V_{GS} > V_{th}$. under visible light irradiation.

charge separation results in a characteristic negative V_{th} shift. Under a negative gate bias ($V_{GS} < V_{th}$), the photogenerated electrons predominantly migrate laterally along the back channel of the IGZO layer at the CQWs/IGZO interface, enabling a detectable photocurrent even without significant gate bias. In the on-state with positive V_{GS} ($V_{GS} > V_{th}$), these photogenerated electrons readily traverse the interface to participate in the external current loop. Once the light is turned off, residual photoelectrons in the IGZO channel and trapped holes in the CQW layer establish an electric field at the CQWs/IGZO interface. This built-in field promotes charge recombination and simultaneously prolongs photoresponse decay, a hallmark of persistent photoconductivity in photo-gated devices [36].

2.5 | Phototransistor–QLED Integration for Optoelectronic Modulation

To demonstrate the practical applicability of the CQWs/IGZO phototransistor, we integrated it with a QLED, forming a functional optoelectronic circuit. Figure 5A illustrates the device architecture, wherein the Al anode of the QLED is electrically connected to the drain terminal of the phototransistor, while the ITO cathode is directly grounded to complete the circuit. This design enables gate-tunable I_D of the phototransistor to dynamically modulate the electroluminescence intensity of the QLED, achieving direct coupling between optical sensing and light emission.

The Al anode (with a work function: ~ 4.3 eV) and ITO cathode (with a work function: ~ 4.7 eV) are strategically chosen to align with the energy levels of the QLED's emissive layer, minimizing interfacial carrier injection barriers and enhancing overall device efficiency [37, 38]. Figure 5B,C demonstrates that systematic modulation of the gate-source bias enables precise regulation of both QLED switching states and gradual tuning of luminescence intensity. Figure S12 presents the output characteristics of the IGZO phototransistor (without integrated QLED) under V_{GS} modulation (V_{GS} = 0–20 V).

Spectral measurements confirm a gate-voltage-dependent enhancement in QLED electroluminescence intensity, exhibiting a monotonic increase in QLED radiant flux with ascending gate potentials. This successful integration validates the device's practical applicability in the active-matrix QLED (AMQLED) architectures, demonstrating the viability of CQWs/IGZO phototransistors for advanced display technologies through gate-programmable optoelectronic coupling mechanisms. The luminous intensity of the QLED can also be tuned by the wavelength of light incident on the CQWs photonic crystals, highlighting the device's application potential (Figure S13 shows the variation curve of I_{DS} at different wavelengths). As illustrated in Figure 5D, the proposed architecture not only demonstrates enhanced photodetection capabilities but also retains robust electrical performance when benchmarked against prior studies, with detailed comparative metrics provided in Table 2.

3 | Conclusions

In summary, we have demonstrated a transformative approach to enhance the visible-light photoresponse of IGZO phototransistors through the integration of 2D CdSe/CdTe/CdSe CQWs via ambient-air-compatible spin-coating process. This heterojunction architecture achieves a specific detectivity of 1×10^{11} Jones at 660 nm, effectively bridging the performance gap between wide-bandgap oxides and narrow-bandgap semiconductors. The key to this performance enhancement lies in the engineered energy-band alignment at the CQW/IGZO interface (ΔE_c = 0.15 eV, ΔE_v = 0.78 eV), which promotes efficient electron–hole separation and directional carrier transport. Gate-voltage modulation enables dynamic tuning of the photoresponse, where negative gate biases amplify photocurrent through enhanced built-in potentials, while positive biases suppress noise via carrier

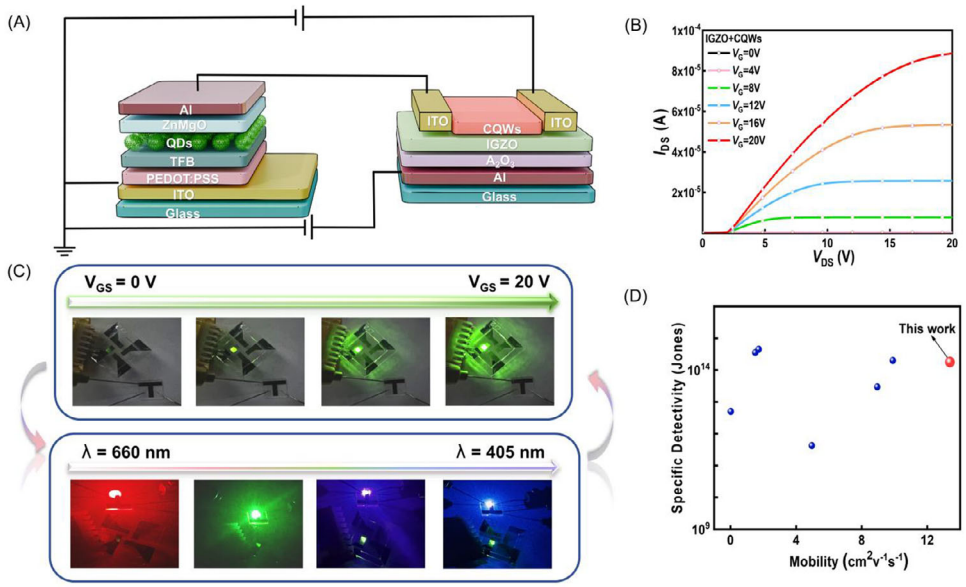

FIGURE 5 | (A) Schematic of the integrated phototransistor-QLED circuit; (B) Output characteristics of phototransistor-driven QLED under gate modulation (V_{GS} = 0–20 V); (C) Optical images of a phototransistor driven QLED at various V_{GS} s and wavelengths (λ = 660 m, 520 nm, 450 nm, 405 nm, P = 2 mW mm^{-2}); (D) Benchmark comparison of our device with previously reported IGZO-based phototransistors. The previous data are acquired from refs. [36, 40, 45, 46, 48].

TABLE 2 | Comparison of IGZO phototransistors with different sensitization layers.

Active layer	μ_{max} ($cm^2V^{-1}s^{-1}$)	Response range (nm)	D^*_{max} (Jones)	PS (I_{photo}/I_{dark})	Inert gas environment	References
IGZO film/CdSe/CdTe/CdSe CQWs	**13.38**	**405–660**	**1.79×10^{14}**	**5.32×10^{8}**	**No**	**This work**
IGZO film/ITON	7.6	450–635	6.43×10^{15}	1.03×10^{7}	Yes (N_2)	[33]
IGZO film/ZnON	<10	450–635	2×10^{14}	10^{6}	Yes (N_2)	[34]
ZnO film/CdSe/ZnS QDs	1.72	405–520	4.5×10^{14}	3.8×10^{7}	/	[36]
IGZO film/$CsPbI_2Br$	/	450–635	8.42×10^{14}	8.71×10^{6}	Yes (N_2)	[39]
IGZO film/IZO	1.51	405–520	3.55×10^{14}	1×10^{7}	No	[40]
WS_2 QDs/rGO-PEDOT:PSS	/	365–800	2.86×10^{11}	/	/	[41]
IGZO film/$BA_2MA_3Pb_4I_{13}$	/	520	5.4×10^{12}	1.3×10^{5}	/	[42]
IGZO film/$CsPbBr_3$	/	457	7.6×10^{13}	$<1 \times 10^{5}$	/	[43]
IGZO film/$CsPbBr_3$ QDs	/	450–550	/	2.51×10^{5}	/	[44]
ZnO film /$FACsPbBr_3$ QDs	/	450–520	1.85×10^{14}	10^{8}	Yes (N_2)	[6]
IGZO film/$CsPbBr_3$ QDs	8.95	500	2.96×10^{13}	/	/	[45]
IGZO film/CdS	0.02	550	5×10^{12}	/	/	[46]
IGZO film/TiO_2	12.14	635	1.25×10^{10}	/	/	[47]
IGZO film/IGZO (sol)	4.96	635	4.23×10^{11}	/	/	[48]

depletion. Finally, the successful integration of the phototransistor integration with a QLEDs demonstrates its viability in active-matrix displays and highlights its potential in adaptive optoelectronic systems. This work opens a promising application for expanding the functionality of wide-bandgap oxide electronics using solution-processable, air-stable quantum well sensitizers.

4 | Experimental Section

4.1 | Phototransistor Preparation

Phototransistor devices were fabricated on quartz glass substrates. First, 300 nm-thick Al-Nd gate electrodes were deposited via magnetron sputtering, patterned using standard photolithog-

raphy, and followed by a 200 nm gate dielectric layer via anodic oxidation. The IGZO active layer was deposited by magnetron sputtering using a ceramic IGZO target (In:Ga:Zn = 2:1:1 at % 4N). The IGZO films were first prepared by radio frequency (RF) sputtering, and a pure argon environment was used to pass argon into the vacuum chamber at a flow rate of 10 sccm during the deposition of the IGZO films. The deposition pressure during sputtering was 1 Pa, the RF sputtering power was set to 80 W, and the sputtering duration was 20 min.

Next, source/drain electrodes were prepared by magnetron sputtering with ITO targets (SnO_2: In_2O_3 = 10: 90 wt.%), and the ITO films were sputtered using direct current (DC) sputtering, which was also carried out in a pure argon environment, with argon being fed into the vacuum chamber at a flow rate of 10 sccm. The deposition pressure during sputtering was 1 Pa, the DC sputtering power was set at 80 W, and the sputtering duration was 25 min.

After patterning, all devices underwent thermal annealing at 300 °C for 30 min in ambient air to enhance film quality and interface properties. Subsequently, the CQWs layer was deposited by spin-coating. A 2 µL aliquot of the pre-prepared CdSe/CdTe/CdSe CQWs dispersion was dropped onto the IGZO TFT surface using a pipette. The sample was then spin-coated using a two-step process: 1000 rpm/min for 5 s, followed by 5000 rpm/min for 30 s, ensuring uniform coverage across the device surface.

4.2 | Synthesis of CdSe/CdTe/CdSe CQWs

The synthesis of the CdSe/CdTe/CdSe CQWs was modified from our previous report [28]. In a typical synthesis, 170 mg cadmium myristate, 12 mg Se, and 15 mL ODE were mixed and degassed at room temperature in a round-bottom flask. The temperature was then set to 230 °C under an inert atmosphere. At approximately 195 °C, 120 mg of $Cd(OAC)_2{\cdot}2H_2O$ was swiftly added. The reaction was maintained at 235 °C for 4 min, and then, at this temperature, a 0.03 M TOP-Te solution in ODE injection was started at a rate of 5 mL/h using a syringe pump. The CdTe absorption peak was tracked to monitor the growth of the CdTe crown layer via UV–vis, and after the desired CdTe crown growth was obtained, injection was stopped. Following the growth of the CdTe layer, the crown growth precursor was changed to a 0.03 M TOP-ODE-Se solution under identical conditions, and injection was maintained until the desired lateral size for the outer CdSe layer was obtained. After the targeted CdSe crown growth was completed, the reaction was terminated by the addition of 1 mL OA. The solution was cooled to room temperature using a water bath, and 5 mL of hexane was injected to increase the solubility of the CQWs. The obtained solution was washed with ethanol at 6000 rpm for 5 min, and the precipitates were re-dissolved in hexane.

4.3 | Fabrication of QLEDs

The cleaned ITO/glass substrates were treated with O_2 plasma for 5 min (70 W). Then, the PEDOT:PSS (Clevios AI 4083) hole injection layer was deposited onto plasma-pretreated ITO/glass substrates via spin-coating (3000 rpm, 40 s) followed by thermal annealing (150 °C, 30 min). All subsequent layer depositions were conducted within a nitrogen-filled glovebox (O_2/H_2O < 0.1 ppm). The TFB (12 mg/mL in chlorobenzene) hole transport layer was deposited via spin-coating (3000 rpm, 40 s) followed by thermal annealing (150 °C, 30 min). Cd-based QD (Green, 10 mg/mL in n-octane) and ZnO (15 mg/mL in ethanol) solutions were sequentially spin-coated at 1500 rpm (40 s) and 2500 rpm (40 s), respectively. Following complete solvent evaporation, the samples were transferred to a high- thermal evaporation system (5×10^{-4} Pa) for patterned Al electrode fabrication (120 nm).

Acknowledgements

This work was supported by Joint Research Funding Program between the Macau Science and Technology Development Fund (FDCT) and the Department of Science and Technology of Guangdong Province (2024) (FDCT-GDST) (No. 0003-2024-AGJ), National Natural Science Foundation of China (62575315), the Guangdong Basic and Applied Basic Research Foundation (2023B1515120046), Guangdong S&T programme (2024A0505090010), Research Fund of Guangdong-Hong Kong-Macao Joint Laboratory for Intelligent Micro-Nano Optoelectronic Technology (2020B1212030010), the Key Laboratory in the Higher Education Institutions of Educational Commission of Guangdong Province (2021KSYS008), the Program for Guangdong High-Level Talents (2021QN02×053), Guangdong Innovation and Entrepreneurship Team Project (2021ZT09×070). The authors gratefully acknowledge the support from Singapore Agency for Science, Technology and Research (A*STAR) MTC program (Grant No. M21J9b0085). Partial support was also provided by TUBITAK 119N343, 120N076, 121C266, 121N395, and 20AG001. H.V.D. would like to acknowledge the support received from the TUBA and TUBITAK 2247-A National Leader Researchers Program (121C266).

Conflicts of Interest

The authors declare no conflicts of interest.

Data Availability Statement

The data that support the findings of this study are available from the corresponding author upon reasonable request.

References

1. H. Yoo, I. S. Lee, S. Jung, et al., "A Review of Phototransistors Using Metal Oxide Semiconductors: Research Progress and Future Directions," *Advanced Materials* 33 (2021): 2006091.

2. J. Mun, H. Kong, J. Lee, et al., "Enhanced Photocurrent Performance of Flexible Micro-Photodetector Based on PN Nanowires Heterojunction using All-Laser Direct Patterning," *Advanced Functional Materials* 33 (2023): 2214950.

3. J. Jie, W. Deng, X. Zhang, and X. Zhang, "A phototransistor with visual adaptation," *Nature Electronics* 4 (2021): 460–461.

4. I. S. Lee, J. Jung, D. H. Choi, S. Jung, K. Kwak, and H. J. Kim, "Novel Method for Fabricating Visible-Light Phototransistors Based on a Homojunction-Porous IGZO Thin Film Using Mechano-Chemical Treatment," *ACS Applied Materials & Interfaces* 13 (2021): 35981–35989.

5. C. Zhang, X. Yin, G. Qian, Z. Sang, Y. Yang, and W. Que, "Gate Voltage Adjusting PbS-I Quantum-Dot-Sensitized InGaZnO Hybrid Phototransistor with High-Sensitivity," *Advanced Functional Materials* 34 (2024): 2308897.

6. M. M. Hasan, E. Moyen, J. K. Saha, M. M. Islam, A. Ali, and J. Jang, "Solution Processed High Performance Perovskite Quantum Dots/ZnO Phototransistors," *Nano Research* 15 (2022): 3660–3666.

7. C. Zhao, M. U. Ali, J. Ning, and H. Meng, "Organic Single Crystal Phototransistors: Recent Approaches and Achievements," *Frontiers of Physics* 16 (2021): 43202.

8. K. Nomura, H. Ohta, A. Takagi, T. Kamiya, M. Hirano, and H. Hosono, "Room-Temperature Fabrication of Transparent Flexible Thin-Film Transistors using Amorphous Oxide Semiconductors," *Nature* 432 (2004): 488–492.

9. T. Kamiya and H. Hosono, "Material Characteristics and Applications of Transparent Amorphous Oxide Semiconductors," *NPG Asia Materials* 2 (2010): 15–22.

10. J. Troughton and D. Atkinson, "Amorphous InGaZnO and Metal Oxide Semiconductor Devices: An Overview and Current Status," *Journal of Materials Chemistry C* 7 (2019): 12388–12414.

11. S. Knobelspies, A. Daus, G. Cantarella, et al., "Flexible a-IGZO Phototransistor for Instantaneous and Cumulative UV-Exposure Monitoring for Skin Health," *Advanced Electronic Materials* 2 (2016): 1600217.

12. E. Lee, T. H. Kim, S. W. Lee, et al., "Improved Electrical Performance of a Sol–Gel IGZO Transistor with High-k Al2O3 Gate Dielectric Achieved by Post Annealing," *Nano Convergence* 6 (2019): 24.

13. A. Sen, H. Park, P. Pujar, et al., "Probing the Efficacy of Large-Scale Nonporous IGZO for Visible-to-NIR Detection Capability: An Approach toward High-Performance Image Sensor Circuitry," *ACS Nano* 16 (2022): 9267–9277.

14. J. H. Ma, J. H. Jeong, S. J. Kang, et al., "High Rejection-Ratio IGZO Ultraviolet Phototransistor via Additional Solution Processed ZnO Absorption Layer," *Advanced Optical Materials* 12 (2024): 2400166.

15. J. Yang, H. Kwak, Y. Lee, et al., "MoS 2 –InGaZnO Heterojunction Phototransistors with Broad Spectral Responsivity," *ACS Applied Materials & Interfaces* 8 (2016): 8576–8582.

16. Y. J. Tak, D. J. Kim, W.-G. Kim, et al., "Boosting Visible Light Absorption of Metal-Oxide-Based Phototransistors via Heterogeneous In–Ga–Zn–O and CH 3 NH 3 PbI 3 Films," *ACS Applied Materials & Interfaces* 10 (2018): 12854–12861.

17. H. Hao, Y. A. Ding, L. Meng, et al., "Broadband and Persistent Photoconductivity Immune Phototransistors Achieved by a Perovskite/IGZO Heterojunction," *ACS Applied Optical Materials* 3 (2024): 223–230.

18. H. M. Ko, S. J. Yang, J. Jeung, et al., "IGZO Phototransistor with Ultrahigh Sensitivity at Broad Spectrum Range (450–950 nm) Realized by Incorporating PM6:Y6 Bulk Heterojunction," *Advanced Optical Materials* 12 (2024): 2303152.

19. J. Kim, J. B. Park, M. G. Kim, et al., "Correlation Between Surface Functionalization and Optoelectronic Properties in Quantum Dot Phototransistors," *IEEE Electron Device Letters* 42 (2021), 553.

20. Y. J. Jeong, G.-B. Kim, M. J. Kim, J. Oh, J.-H. Chang, and J. K. Jeong, "Improvement in Performance and Stability of PbS QD/IGZO Phototransistors Through the Introduction of Ga 2 O 3 Film for Broadband Sensor Applications," *ACS Applied Materials & Interfaces* 16 (2024): 36527–36538.

21. Y. Zou, W. Yu, H. Guo, et al., "A crystal Capping Layer for Formation of Black-Phase FAPbI 3 Perovskite in Humid Air," *Science* 385 (2024): 161–167.

22. B. Liu, Y. Altintas, L. Wang, et al., "Record High External Quantum Efficiency of 19.2% Achieved in Light-Emitting Diodes of Colloidal Quantum Wells Enabled by Hot-Injection Shell Growth," *Advanced Materials* 32 (2020): 1905824.

23. S. Delikanli, O. Erdem, F. Isik, et al., "Ultrahigh Green and Red Optical Gain Cross Sections from Solutions of Colloidal Quantum Well Heterostructures," *The Journal of Physical Chemistry Letters* 12 (2021): 2177–2182.

24. E. V. Shornikova, D. R. Yakovlev, N. A. Gippius, et al., "Exciton Binding Energy in CdSe Nanoplatelets Measured by One- and Two-Photon Absorption," *Nano Letters* 21 (2021): 10525–10531.

25. S. Hu, F. Shabani, B. Liu, et al., "High-Performance Deep Red Colloidal Quantum Well Light-Emitting Diodes Enabled by the Understanding of Charge Dynamics," *ACS Nano* 16 (2022): 10840–10851.

26. J. Yu, E. G. Durmusoglu, Y. Wang, M. Sharma, H. V. Demir, and C. Dang, "Ultrafast Control of the Optical Transition in Type-II Colloidal Quantum Wells," *ACS Photonics* 10 (2023): 1250–1258.

27. E. G. Durmusoglu, S. Hu, P. L. Hernandez-Martinez, et al., "High External Quantum Efficiency Light-Emitting Diodes Enabled by Advanced Heterostructures of Type-II Nanoplatelets," *ACS Nano* 17 (2023): 7636–7644.

28. S. Delikanli, B. Canimkurbey, P. L. Hernández-Martínez, et al., "On the Rational Design of Core/(Multi)-Crown Type-II Heteronanoplatelets," *Journal of the American Chemical Society* 145 (2023), 12033.

29. E. B. Aydın and M. K. Sezgintürk, "Indium Tin Oxide (ITO): A Promising Material in Biosensing Technology," *TrAC Trends in Analytical Chemistry* 97 (2017): 309–315.

30. C. Shen, Z. Yin, F. Collins, and N. Pinna, "Atomic Layer Deposition of Metal Oxides and Chalcogenides for High Performance Transistors," *Advanced Science* 9 (2022): 2104599.

31. Y. Huang, E.-L. Hsiang, M.-Y. Deng, and S.-T. Wu, "Mini-LED, Micro-LED and OLED Displays: Present Status and Future Perspectives," *light: science & applications* 9 (2020): 105.

32. D.-B. Ruan, P.-T. Liu, Y.-H. Chen, et al., "Photoresponsivity Enhancement and Extension of the Detection Spectrum for Amorphous Oxide Semiconductor Based Sensors," *Advanced Electronic Materials* 5 (2019): 1800824.

33. K. Jang, Y. Jang, S. An, and S.-Y. Lee, "In-Situ IGZO/ITON Heterostructure Phototransistor to Enhance Visible Light Detection," *IEEE Electron Device Letters* 45 (2024): 1839–1842.

34. Y. Jang and S. Y. Lee, "In Situ IGZO/ZnON Phototransistor Free of Persistent Photoconductivity with Enlarged Spectral Responses," *ACS Applied Electronic Materials* (2022): 509–519.

35. T. Chen, S. Zhan, B. Li, B. Hou, and H. Zhou, "A Low-Toxic Colloidal Quantum Dots Sensitized IGZO Phototransistor Array for Neuromorphic Vision Sensors," *Advanced Optical Materials* 12 (2024): 2302451.

36. S. Park, B. J. Kim, T. Y. Kim, et al., "Improving the Photodetection and Stability of a Visible-Light QDs/ZnO Phototransistor via an Al 2 O 3 Additional Layer," *Journal of Materials Chemistry C* 9 (2021): 2550–2560.

37. Y. Yu, Y. Liang, J. Yong, et al., "Low-Temperature Solution-Processed Transparent QLED Using Inorganic Metal Oxide Carrier Transport Layers," *Advanced Functional Materials* 32 (2022): 2106387.

38. W. Ji, T. Wang, B. Zhu, et al., "Highly Efficient Flexible Quantum-Dot Light Emitting Diodes with an ITO/Ag/ITO Cathode," *Journal of Materials Chemistry C* 5 (2017): 4543–4548.

39. H.-J. Na, N.-K. Cho, J. Park, et al., "A Visible Light Detector Based on a Heterojunction Phototransistor with a Highly Stable Inorganic CsPbI x Br 3−x Perovskite and In–Ga–Zn–O Semiconductor Double-Layer," *Journal of Materials Chemistry C* 7 (2019): 14223–14231.

40. Y. B. Kim, J. H. Jeong, M. H. Park, et al., "Low-Power Phototransistor with Enhanced Visible-Light Photoresponse and Electrical Performances Using an IGZO/IZO Heterostructure," *Materials* 17 (2024): 677.

41. P. Hao, W. Jiang, M. Li, et al., "Fully Flexible Yarn-Based Phototransistors for UV–Visible Light Detection," *ACS Photonics* 11 (2023): 128–138.

42. T. Chen, C. Wang, G. Yang, et al., "Monolithic Integration of Perovskite Photoabsorbers with IGZO Thin-Film Transistor Backplane for Phototransistor-Based Image Sensor," *Advanced Materials Technologies* 8 (2023): 2200679.

43. Y. Hou, L. Wang, X. Zou, et al., "Substantially Improving Device Performance of All-Inorganic Perovskite-Based Phototransistors via Indium Tin Oxide Nanowire Incorporation," *Small* 16 (2020): 1905609.

44. Z. Xin, Y. Tan, T. Chen, et al., "Visible-Light-Stimulated Synaptic InGaZnO Phototransistors Enabled by Wavelength-Tunable Perovskite Quantum Dots," *Nanoscale Advanced* 3 (2021): 5046–5052.

45. H. Yu, X. Liu, L. Yan, et al., "Enhanced UV–Visible Detection of InGaZnO Phototransistors via CsPbBr 3 Quantum Dots," *Semiconductor Science and Technology* 34 (2019): 125013.

46. C. H. Ahn, Y. K. Kim, W. J. Kang, K. S. Kim, and H. K. Cho, "High Photosensitivity and Wide Operation Voltage in Two-Dimensional CdS Nano-Crystal Layer Embedded a-InGaZnO Hybrid Phototransistors," *Journal of Alloys and Compounds* 725 (2017): 891–898.

47. D. Kim, Y.-G. Kim, B. H. Kang, J. H. Lee, J. Chung, and H. J. Kim, "Fabrication of Indium Gallium Zinc Oxide Phototransistors via Oxide-Mesh Insertion for Visible Light Detection," *Journal of Materials Chemistry C* 8 (2020), 165–172.

48. J. Chung, Y. J. Tak, W.-G. Kim, B. H. Kang, and H. J. Kim, "Artificially Fabricated Subgap States for Visible-Light Absorption in Indium–Gallium–Zinc Oxide Phototransistor with Solution-Processed Oxide Absorption Layer," *ACS Applied Materials & Interfaces* 11 (2019): 38964–38972.

Supporting Information

Additional supporting information can be found online in the Supporting Information section.

Supporting File: lpor70561-sup-0001-SuppMat.docx.